

A near-infrared, optical and ultraviolet polarimetric and timing investigation of complex equatorial dusty structures

F. Marin^{*}, P. A. Rojas Lobos, J. M. Hameury, and R. W. Goosmann

Université de Strasbourg, CNRS, Observatoire astronomique de Strasbourg, UMR 7550, F-67000 Strasbourg, France

Received 15 December, 2017; Accepted 23 January 2018

ABSTRACT

Context. From stars to active galactic nuclei, many astrophysical systems are surrounded by an equatorial distribution of dusty material that are, in a number of cases, spatially unresolved even with cutting edge facilities.

Aims. In this paper, we investigate if and how one can determine the unresolved and heterogeneous morphology of dust distribution around a central bright source using time-resolved polarimetric observations.

Methods. We use polarized radiative transfer simulations to study a sample of circumnuclear dusty morphologies. We explore a grid of uniform, fragmented, density-stratified, geometrically-variable models in the near-infrared, optical and ultraviolet bands, and present their distinctive time-dependent polarimetric signatures.

Results. As expected, varying the structure of the obscuring equatorial disk has a deep impact on the inclination-dependent flux, polarization degree and angle, and time-lags we observe. We find that stratified media are distinguishable by time-resolved polarimetric observations, and that the expected polarization is much higher in the infrared band than in the ultraviolet. However, due to the physical scales imposed by dust sublimation, the average time-lags between the total and polarized fluxes are important (months to years), lengthening the observational campaigns necessary to break more sophisticated (and therefore also more degenerated) models. In the ultraviolet band, time-lags are slightly shorter than in the infrared or optical bands, and, coupled to lower diluting starlight fluxes, time-resolved polarimetry in the UV appears more promising for future campaigns.

Conclusions. Equatorial dusty disks differ in terms of inclination-dependent photometric, polarimetric and timing observables, but only the coupling of these different markers can lead to inclination-independent constraints on the unresolved structures. Polarized reverberation mapping in the ultraviolet/blue band, despite being complex and time-consuming, is probably the best technique to rely on in this field.

Key words. Galaxies: active – Polarization – Radiative transfer – Scattering – (Stars:) circumstellar matter – Stars: general

1. Introduction

Dusty disks are detected in a variety of astronomical sources that range from stars to the innermost regions of active galactic nuclei (AGN). A disk¹ naturally forms when matter with sufficient angular momentum is accreted onto a central object, regardless if it is a star, a neutron star or a black hole. We know that dust grains can form at the outer rim of AGN and young stars accretion disks (Mundy et al. 1993; D’Alessio et al. 1998, 1999; Czerny & Hryniewicz 2012) and the fact that disks are ubiquitous in the Universe naturally provides clues to the physics of accretion in various environments. By studying dust disks, we can put strong constraints on the formation mechanisms of dust grains, and how they survive and evolve.

Equatorial dusty mixtures can be probed locally, i. e. within the Galaxy, by observing stars. It is thought that almost all stars are born with circumstellar disks (Beckwith & Sargent 1996; Hillenbrand et al. 1998). Young stars often show protoplanetary disks, which are a collection of material left over from the stellar formation process. In Keplerian orbit, this circumstellar, flared region contains both gas and dust (with a gas to dust ratio of ~ 100 , Beckwith et al. 1990). While the exact composition of dust in protoplanetary disks is poorly known, silicates and amor-

phous carbons covered by icy mantles are favored (e.g., Pollack et al. 1994 or, more recently, Jones 2016). After the accretion stage of the young stellar object, the dust mixture in the disk continues to evolve. The innermost grains start to collide and stick together, forming larger grains that sink towards the disk mid-plane due to the vertical component of gravity. Substantial dust settling can profoundly alter the geometry of the protoplanetary disk: the photosphere of the disk is dragged down with the dust (Dubrulle et al. 1995; Schröpfer & Henning 2004). Turbulence, if any, tends to mix the grains back up again, resulting in non-homogeneous equatorial structures around the star that can be probed in the mid and far-infrared, where dust thermally re-emit (Dullemond et al. 2007).

The infrared re-emission of dust was used to infer the existence of dusty disks around more evolved stars, such as cool, old white dwarfs in planetary nebulae (Farihi et al. 2009; Clayton et al. 2014). A dust-related infrared excess was first discovered around the Helix planetary nebula by Su et al. (2007) and later surveys have found several other dust-encircled candidates (Chu et al. 2011). The $24 \mu\text{m}$ flux densities of hot white dwarfs and central stars of planetary nebula is more than two orders of magnitude higher than their expected photospheric emission, revealing the presence of cold dust disks (Chu et al. 2011). The disk, in those cases, may derive from the AGB phase of the star evolution (Clayton et al. 2014) or collisions of Kuiper belt-like object (Bilíková et al. 2012). It is not easy to distinguish between the two formation mechanisms as the system is not fully resolved.

^{*} e-mail: frederic.marin@astro.unistra.fr

¹ Collimated polar outflows, quasi-spherical winds and jets can also form during accreting periods but it is beyond the scope of this paper to treat them.

Disk sizes are hard to measure because the outer parts are cool and emit weakly, but it is thought that circumstellar disks extend up to a few hundreds of astronomical units (see, e.g., Vicente & Alves 2005). The inner part of the dusty disk is set up by the sublimation radius that depends on the dust composition and temperature of the central source (Kishimoto et al. 2007). Current millimeter and sub-millimeter/interferometers provide images of the dust and gas outer disks with an angular resolution better than $1''$ (i.e. 150 AU at the distance of the nearest star forming regions). As an example, the Atacama Large Millimeter/submillimeter Array (ALMA) can reach a resolution of $0.5''$ at 950 GHz in its most compact 12-m array configurations. Using longer baselines (up to 14 km), Andrews et al. (2016) successfully traced millimeter-sized particles down to spatial scales as small as 1 AU (20 mas).

High angular resolution observations can also be obtained in the K and N bands, with the Keck Interferometer (Eisner et al. 2007) and the Very Large Telescope Interferometer (Jaffe et al. 2004), respectively. The former authors successfully resolved the circumstellar material $2.2 \mu\text{m}$ emission within the first astronomical unit around young stars. The later spatially resolved a parsec-sized torus-shaped distribution of dust grains in the Seyfert galaxy NGC 1068. This circumnuclear dust region was for long invisible to our instruments and is now at the edges of the resolution capabilities of current telescopes (Beckert et al. 2008). However, the true morphology and composition of this equatorial region is still largely unknown; it would require to resolve sizes inferior to a fraction of a parsec at mega-parsec distances. We thus need to find another observation technique to reveal the geometry of unresolvable dusty disks, either around young stars or supermassive black holes.

Indirect techniques such as Doppler tomography (Marsh & Horne 1988) or eclipse mapping (see e.g. Horne 1985) have been widely used for cataclysmic variables, but these are restricted to binary systems and cannot be applied to isolated stars or AGN. Another very successful method that can go beyond the resolution capabilities of current telescopes is the observation of polarized light. Polarization has proven to be independent of the size of the emitting/scattering region. Only the observed polarization degree and position angle are sensitive to the morphology, composition and magnetic fields of the media that can emit, scatter or absorb photons. Observing the polarized light of NGC 1068, Antonucci & Miller (1985) successfully unveiled the broad emission lines that were undetectable in the total flux spectrum. Those lines, obscured by the equatorial distribution of dust around active galactic nuclei cores, were only revealed thanks to near-infrared, optical and ultraviolet spectropolarimetry. They laid the foundations of the unified model of AGN (Antonucci 1993). Polarimetry is also extremely powerful in detecting dusty equatorial structures around bright stars. The polarized light, emerging from scattering of stellar photons on the disk surface, shaves off the unpolarized contribution from the central star. After correcting for stellar starlight dilution only the disk emission is detected thanks to its contrast. Imaging polarimetry then allows to reveal the disk inner regions down to a few astronomical units (see, e.g., Gledhill et al. 1991; Apai et al. 2004).

Now that we are able to detect the polarized signatures of dusty disks (at least around stars, not yet for AGN), it is of prime importance to determine their true structure. Models from the literature almost systematically use plain, uniform, constant density disks since they are easier to explore numerically. A simple geometry, reducing the model parameter space, is much less time-consuming when radiative transfer or magneto-

hydrodynamical simulations are used. Density-variations have been sometimes included (see, e.g., Walker et al. 2004; Pinte et al. 2009) and already revealed a number of photometric and spectroscopic differences with respect to constant-density disks. The same conclusion applies to the disk geometry (Nenkova et al. 2002; Marin et al. 2015). Flared or cylindrical disks are the two most common morphologies used in simulations but it has been shown that the structure of circumstellar and circumnuclear disks is more complex. Clumpy dusty structures have been detected around stars and brown dwarfs (e.g., in the σ Ori cluster, see Scholz et al. 2009), as well as from galactic structures (e.g., in NGC 4244, see Holwerda et al. 2012). Even if the parsec-scale dust disk around the core of AGN has not yet been resolved to the point of detecting individual clumps, hydrodynamical models predict that large homogeneous distributions of dust cannot be stable (Krolik & Begelman 1988). Various indirect evidences for the clumpiness of AGN tori are detected in the X-rays, where fluorescent line emission (Liu et al. 2016) and variations in the obscuring column density of edge-on Seyferts (Marinucci et al. 2016) strongly suggest a non-uniform equatorial torus morphology.

It is the aim of this paper to investigate in great details the different morphologies and density stratifications of equatorial dusty disks. By doing so, we want to check whether near-infrared, optical and ultraviolet polarimetry can shed light on the true geometry of those unresolvable regions. We consider disk parameters (in particular disk sizes) appropriate for AGN, but our results can be easily extrapolated to different environments. We thus study very realistic models of dusty environments that exist in accreting objects and present the radiative transfer code we used in Sect. 2. We compile and discuss our results in Sect. 3, where the photometric flux, polarization degree, polarization angle and time-lags for each of the fifteen models are presented. We analyze the benefits, problems and the limitations of polarized time reverberation studies in Sect. 4 by comparing our conclusions to recent observations, and we conclude our paper in Sect. 5.

2. Models of equatorial dusty structures

In the following, we use for a geometrical configuration that matches the observational constraints for AGN. Our goal is not to precisely model a circumstellar or a circumnuclear disk. We instead test the impact of different geometries and compositions onto the resulting photometric flux, polarization and time-lags. We consider throughout this paper a flared disk with inner radius 0.1 pc and outer radius 10 pc. The first value corresponds to the inner radius set by dust sublimation theories for a typical Seyfert galaxy whose dust is mainly composed of graphite and silicate grains (Kishimoto et al. 2007). The outer radius is the typical torus extension set by modeling constraints based on spectroscopic and interferometric observations and is of order of 5 – 10 pc (Meisenheimer et al. 2008; Burtscher & Tristram 2013; Netzer 2015; López-Gonzaga & Jaffe 2016). The half-opening angle of the flared disk is set to 45° . This corresponds to the estimated torus height derived from quasar observations (Sazonov et al. 2015), numerical modeling (Marin et al. 2012; Gnedin et al. 2015), and statistical analyses (Marin 2014, 2016).

2.1. Dusty disks with increasing complexity

We show in Fig. 1 the six different disk geometries we investigate in this paper. We consider first a plain flared disk that is uniformly filled with dust. Its radial optical depth in the V-band

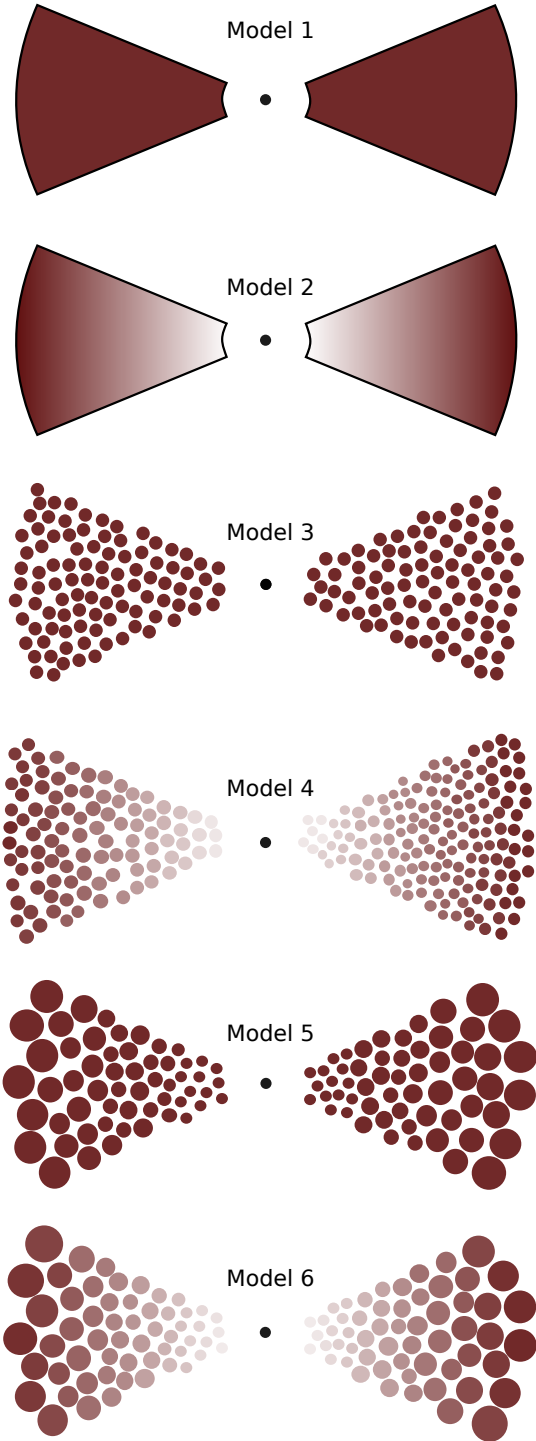


Fig. 1. Unscaled geometrical and density variations for our models of dusty disks. The first two panels show a model with a uniform geometry and the last four panel a set of fragmented disks. A uniform red filling indicates a constant optical depth, while a color gradient indicates a variation in the dust density with increasing radial distances from the central source. Details are given in the text.

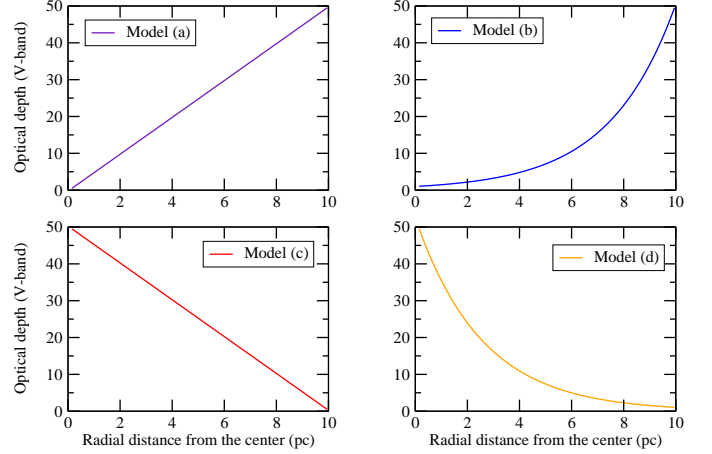


Fig. 2. Theoretical dust distributions corresponding to heterogeneously-filled dust disks. Each model is color-coded and shows a different variation of the radial optical depth (in the V-band) with increasing distance from the central source. Details are given in the text.

is larger than 100 to ensure a strong obscuration along the equatorial plane (Antonucci 1993). This is the simplest configuration and it is one of the most used in numerical simulations. Model number 2 is also a plain flared disk but its dust density varies with radial distance from the central source. The third model is a clumpy flared disk with clumps of equal sizes and density. Each clump has an optical depth of 50 (Siebenmorgen et al. 2015) and 7 to 10 clumps are obstructing the observer’s line-of-sight along equatorial views, ensuring a total optical depth equal to or larger than 100. Its non-homogeneously filled counter-part is model 4, where the dust density varies with the radial distance from the center. Finally, model number 5 is a clumpy disk with clump sizes becoming bigger and bigger as we move away from the center. A clump located at the outer part of the structure is ten times larger than a clump located at the inner edge. In this model the dust density is inversely proportional to the clump radius so that each cloud has a constant optical depth of 50 in the V-band. The last model is the same as model 5 but the dust optical depth is no longer constant.

The different distributions of dust used in models 2, 4 and 6 are presented in Fig. 2. We consider four dust distributions, defined by their optical depth in the V-band plotted as a function of the radial distance from the central black hole. The size of the disks being the same for all models, the change in optical depths is only due to variations in dust densities. Model (a) corresponds to a linear increase of the optical depth with increasing distances from the central source. Model (b) is for an exponential growth. Model (c) and (d) follow the inverse trend, with model (c) being a linear decrease of the dust optical depth with increasing distances from the center, and model (d) an exponential decrease. We therefore have fifteen different test cases: model 1, models 2(a – d), model 3, models 4(a – d), model 5 and models 6(a – d).

We sample 2000 clumps for each clumpy model, equating to a disk filling factor of $\sim 25\%$. The impact of the number of clumps has been studied in Marin et al. (2015) and it was found that the lower the filling factor, the lesser the observed polarization and the higher the total flux. Using a filling factor of $\sim 25\%$ allows for a flux decrease between the polar and equatorial in-

clinations of, at least, one order of magnitude. For all models, we fix the dust composition to the Milky Way mixture (Wolf & Henning 1999). This is the standard dust composition observed in the solar neighborhood, but different mixtures can reside in different systems, such as postulated by Gaskell et al. (2004) and Li (2007). In the Milky Way, the dust is essentially composed of 62.5% carbonaceous dust grains and 37.5% astronomical silicate. Both ortho- and para-graphite are considered, with twice as much para-graphite as ortho-graphite (Wolf & Henning 1999). The grain size distribution ranges from $0.005 \mu\text{m}$ to $0.250 \mu\text{m}$ in radii, with a distribution $n(a) \propto a^s$ and $s = -3.5$. Varying the dust grain radius distribution or the dust composition will result in a different albedo, hence different scattered/absorbed fluxes and polarization. However, in the following, we always compare models with the same dust mixture. The exact dust prescription is then of no importance since we are looking at model differences and not quantitative values. Finally, i is the disk inclination, i.e. the angle between the observer line of sight and the symmetry axis of the disk. Pole-on view corresponds to $i = 0^\circ$, edge-on view to $i = 90^\circ$.

2.2. Polarized radiative transfer

We used the radiative transfer code `STOKES` to achieve our simulations. Developed by Goosmann & Gaskell (2007) and upgraded by Marin et al. (2012, 2015), `STOKES` is a Monte Carlo code that simulates the propagation of radiation in a user-defined three-dimensional environment. The code is extensively detailed in the three papers of the series and we only give here a brief summary of its important features. A list of applications of `STOKES` can be found in Marin & Goosmann (2014).

`STOKES` can model a large range of geometrical shapes that can be filled with electrons, dust grains, atoms and molecules. Emitting regions can be parametrized as sources with a given spectral shape. Photons, once emitted, travel along straight lines until a reprocessing event happens, depending on the optical depth of the media (calculated as $\tau = \int_0^z \sigma n(z) dz$, $n(z)$ being the number density of that material at z , and σ the attenuation cross section). Photons can scatter, be absorbed and be re-emitted in all directions according to the Mie, Rayleigh, Thomson or Compton laws. Multiple scattering can occur and the four components of the Stokes vector are modified at each scattering event. A spherical web of virtual detectors registers each escaping photon, saving its polar and azimuthal coordinates together with the intensity, polarization (linear and circular) and time-lag. The polarization we measure is the scattering-induced, linear, continuum polarization degree ranging from 0 (unpolarized) to 100% (fully polarized). The code can be parallelized and it takes a few days on a basic computer for a computation such as presented in this paper to sample 10^{10} photons.

In the following, we ran our models for three different wavebands: near-infrared (mono-energetic photon emission centered at $10\,000 \text{ \AA}$), optical (5500 \AA), and ultraviolet (2000 \AA). Since the scattering phase function of dust is energy-dependent, we aim to find which is the best suited waveband for a polarimetric detection of the specific features of complex dusty disks. The polarimetric results we present are entirely due to scattering. We do not account for external dilution by the host galaxy, stellar starlight or thermal reprocessing by dust grains. This might have an effect on the polarization signatures, particularly in the infrared domain where dilution by the host galaxy is much more important than in the ultraviolet band (see, e.g., Bolzonella et al.

2000), and it will be discussed in Sect. 4. We registered the flux, polarization and time-lag along 40 polar directions (from the symmetry axis of the model to the equatorial plane) equally spaced in cosine. We azimuthally integrated the signal to get better statistics. It was shown in Marin et al. (2015) that, even for a clumpy distribution, an azimuthally-averaged value is representative of the system provided it is not highly non-axisymmetric.

3. Results

3.1. Uniform disks

We present our first results in Fig. 3, Fig. 4 and Fig. 5 for the near-infrared, optical and ultraviolet bands, respectively. They corresponds to models 1 (plain, uniformly-filled dusty flared disk) and 2 (plain disks with radial dust stratification). We investigate, in model 2, all four dust prescriptions (a), (b), (c), and (d) according to Fig. 2.

3.1.1. Radiation path

Because of the large disk optical depth resulting in multiple scattering, the radiation path is not straightforward. Photons may scatter more than twice before reaching the observer, especially if the disk is clumpy. We illustrate in Fig. 6 the different trajectories the photons can have.

The top panel illustrates the case of an observer situated almost along the symmetry axis of the system, i.e. along the polar direction. In this case, there is a direct view of the central source and photons may travel freely towards the observer (dotted orange line). This is the direct flux, which is unpolarized. If photons are emitted along the equatorial plane, they will encounter the disk funnel (dashed pink line). If not absorbed, they may scatter backward and be reprocessed onto the opposite funnel side until being absorbed or being able to escape. Due to the non-isotropic scattering phase function of Mie scattering, photon can also penetrate further into the disk (long-dashed cyan line). Radiation will scatter at different position before escaping at large distances from the central source. Depending on the position of the last scattering event, its polarization position angle can be either parallel or perpendicular. For the remainder of this paper, we consider that a polarization position angle of 90° indicates a polarization angle parallel to the projected symmetry axis of the disk. This is the signature of equatorial scattering. A polarization angle of 0° is thus perpendicular to the model axis and traces scattering event happening preferentially close to the pole of the model. Note that when a model is perfectly axisymmetric, the polarization angle can only take two values, 0° or 90° . Otherwise, as in the case of a distribution of clumps, various polarization angles can be obtained, related to the statistics of the clumps.

The bottom panel of Fig. 6 illustrates the case of an almost edge-on inclination. The central source is obscured by dust and no longer visible. Photons can escape via multiple scattering along the equatorial plane if the dusty medium is not too optically thick or if there are gaps between the clouds (green long-dashed line). The majority of radiation will preferentially scatter onto the disk surface opposite to the observer and then reach the detectors. This could happen with only one scattering event, where photon is emitted at an angle coincident to the half-opening angle of the disk (dotted blue line), or due to multiple scattering (dashed red line). When the inclination of the system is close to 90° , the obscuration is maximal and the amount of

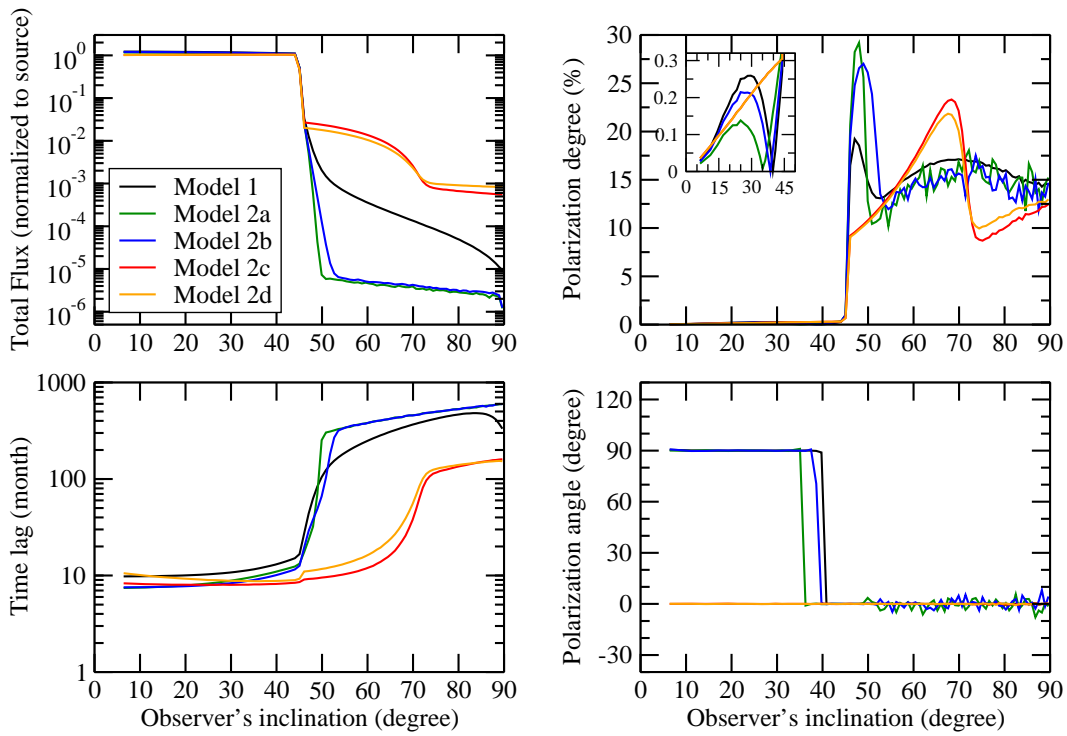


Fig. 3. Near-infrared ($10\,000\text{ \AA}$) total flux (normalized to the source emission), polarization degree, polarization angle and time-lag (normalized to the size of the disk) as a function of the observer's inclination. Five plain flared disk models with different dust distributions are presented (see Sect. 2.1 for details).

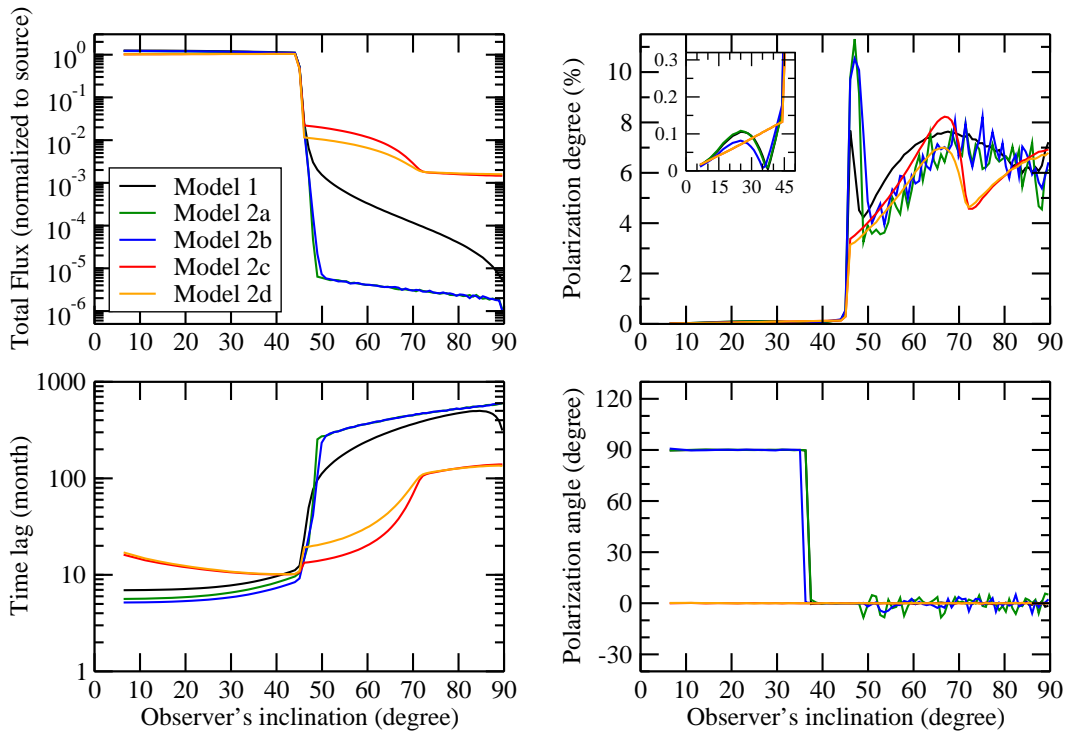


Fig. 4. Same as Fig. 3 but in the optical band (5500 \AA).

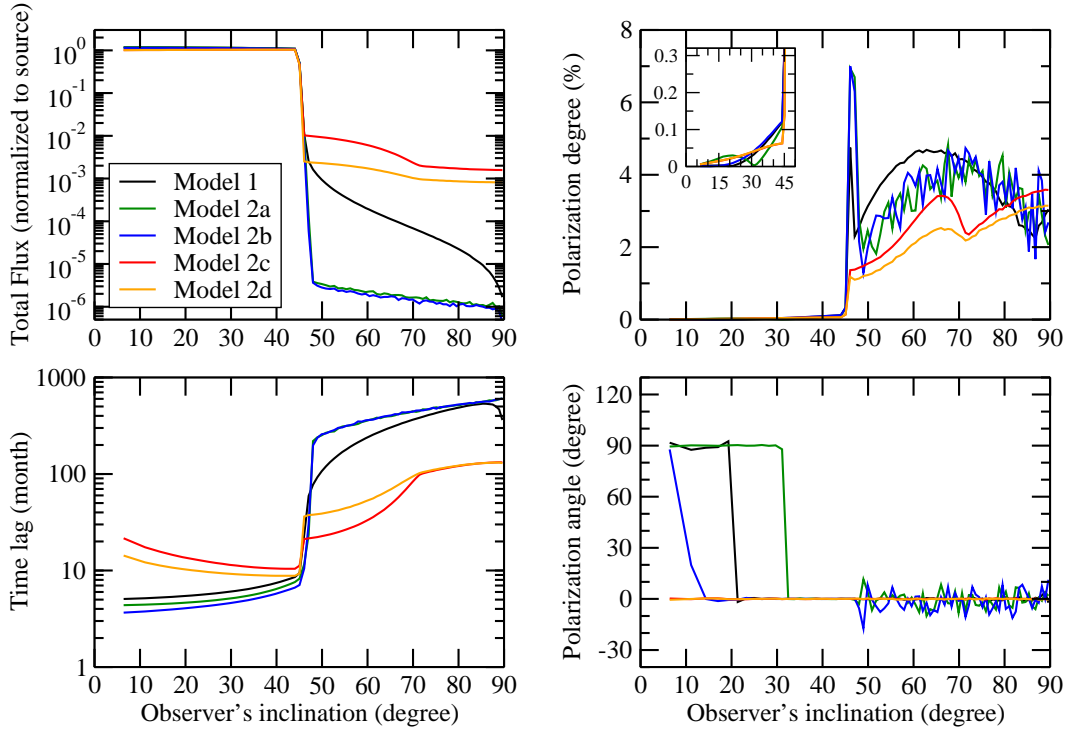


Fig. 5. Same as Fig. 3 but in the ultraviolet band (2000 Å).

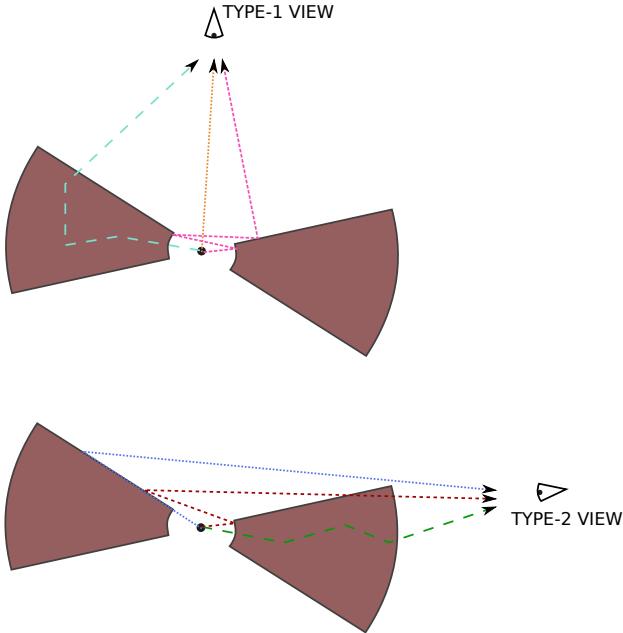


Fig. 6. Illustration of different photon paths due to multiple scattering. See text for details. Top: pole-on (type-1) view, bottom: edge-on (type-2) view.

photons that have backscattered onto the disk surface opposite to the observer (blue and red lines) is minimal.

3.1.2. Total flux

Focusing first on the normalized photon flux (top-left panel of Figs. 3, 4 and 5), we see an almost inclination-independent flux value until the observer's line-of-sight becomes obstructed by the dusty disk. The central source being unobscured, there is little contribution from the flared disk that absorbs/scatters a small fraction of radiation. Nonetheless, models 2(c) and 2(d) present a slightly smaller (by a factor 1.3) flux at those inclinations. The optical depth being maximum at the inner disk radius (see Fig. 2), radiation is more heavily absorbed. Thus, there is less photon scatter toward the polar axis than for the other cases. Once the dusty material intercepts the observer's line-of-sight, the flux drops by several orders of magnitude. For a plain disk where density decreases with radial distances from the center (models (c – d)), the minimum flux is about three orders of magnitude lower than at face-on inclinations. Radiation that successfully crossed the first, dense layers of the inner disk region can freely propagate towards the disk outer radius. The number of photons is thus higher than in the case of a disk with a constant-density profile (model 1). Here, the flux drops by five orders of magnitude and the attenuation is almost linear with inclination. The attenuation is even stronger for the last two models (a – b) when the dust density increases with radial distances from the source, the flux obscuration is very efficient. Between $i = 45^\circ$ and $i = 50^\circ$, the flux sharply drops by five orders of magnitude and then stays constant at edge-on inclinations. In this specific case, photons have traveled far inside the dusty material before encountering the densest layers of dust. Radiation then becomes trapped inside the dust disk and naturally suffers from heavy absorption caused by multiple scattering. The emerging

flux at edge-on inclinations is thus extremely weak as compared to the source.

As the photon energy increases, models (c – d) with decreasing radial optical depth from the center of the disk show a slightly higher edge-on normalized flux, while it is the opposite for the other cases. This complex behavior is related to the albedo and the scattering and extinction cross sections of dust. The albedo is flat in the optical band but decreases in the ultraviolet and infrared regimes. On the other hand, the scattering cross-section decreases regularly with wavelength. An illustration is given in Fig. 3 in Goosmann & Gaskell (2007). The combination of the two factors allows ultraviolet radiation to cross a thicker layer of dust close to the inner radius of the disk: more ultraviolet photons can penetrate the disk, but they get more scattered or absorbed than optical or infrared photons. However, in the case of a model with increasing dust density with radial distance from the source, the first layers of dust being optically then, the same ultraviolet photons will have traveled farther inside the dusty material before being absorbed or scattered. Scattered photons will more easily escape along the polar direction, where the remaining optical depth is smaller, rather than towards the equatorial plane where the optical depth is higher. This results in a decrease of the observed flux even at higher photon energies.

3.1.3. Polarization properties

The polarization properties of the five models (right panels of Figs. 3, 4 and 5) strongly differ both in terms of polarization degree and polarization position angle. At polar inclinations, the degree of polarization is always small, less than a percent. This is due to the strong dilution effect of the unpolarized primary source that outshines the reprocessed component. The polarization degrees are marginally dependent on the half-opening angle of the disk (Marin et al. 2012) but are very sensitive to its composition. There are however differences between models, even for low inclinations. As it can be seen in the small zoom-box inside the polarization degree panels, a uniformly-filled dusty disk produces the highest polarization degrees, while a disk with a linear increase of the dust density with radial distance from the center has the lowest continuum polarization. If the dust density decreases with radial distances (models (c) and (d)), the degree of polarization linearly increases with inclination until $i = 45^\circ$. From 0° to 45° , the other three models show a non-linear variation of their polarization properties, a behavior that is strongly impacted by the amount of reprocessed flux, hence by the model itself. This can be clearly seen when considering the intrinsic polarization position angle. When the dust density is constant or increases with radial distance from the center, the polarization angle is 90° whereas it is 0° otherwise. The first three models are dominated by scattering along the equatorial plane, producing a parallel polarization angle, until the line-of-sight of the observer is obscured by the dusty medium. Scattering then occurs along the polar directions, where photons reprocess on the flared disk surface opposite to the observer's position, see Fig. 6. The polarization angle naturally rotates and the transition between the two polarization states causes the polarization degree to decrease around $i = 45^\circ$ (the half-opening angle of the flared disk). When the disk optical depth decreases with radial distances from the source, the inner edge of the disk is similar to a thick wall of dust and radiation preferentially scatters along the polar direction if it is to escape from the disk, hence the perpendicular polarization angle.

As soon as the source is no longer directly visible by the observer, the polarization angle is fixed for all models (0°) and the polarization degree rises due to Thomson laws. In the case of a uniformly-filled plain flared disk, the maximum infrared polarization degree is $\sim 20\%$ at $i = 50^\circ$, where polar scattering dominates. The polarization then decreases with increasing inclinations, as it becomes more and more difficult for radiation to escape the dust funnel, except by multiple scattering which will induce a natural depolarization effect. In the case of models 2(a) and 2(b), the maximum of polarization (27 – 29%) is reached for inclinations close to 45° . The polarization degree then decreases for the same reasons as before, but the final edge-on value is lower than in the previous case. This is due, as explained above, to the confinement of radiation inside the flared disk and the subsequent heavy absorption. It also explains the lower statistics at edge-on inclinations. Finally, for the last two models in which the dust density decreases with radial distances from the center, the polarization degree peaks at inclinations close to 70° . The maximum infrared polarization is as high as 23%, and then decreases at equatorial orientations, with a polarization level similar to the uniformly-filled case. We thus see that the maximum polarization degree from a plain flared disk occurs for different inclinations and strongly depends on the radial distribution of dust. We see similar behaviors in terms of polarization angles and polarization degrees for all three wavebands considered here, with the polarization degrees decreasing at bluer wavelengths. We also note that the rotation of the polarization position angle of model 2(a) occurs at slightly different inclinations for different energies. Those two phenomena are due to the increase of the dust scattering cross section with decreasing wavelengths.

3.1.4. Time lags

The last panel of Figs. 3, 4 and 5 (bottom-left) represents the averaged time-lag between actual photons reaching the observer and photons emitted by the central source that would not have suffered any scattering. Direct emission has a time-lag of zero. This quantity, with respect to the previous ones, is not directly observable as real cosmic photons are emitted at different times. The true averaged time lags must be reconstructed from observations by comparing polarized and primary light curves through theoretical transfer functions. The time-lags we present therein is to be used as a time indicator of the complexity of the radiation paths and the difficulty photons can have to escape from the dusty disk.

We see that, for pole-on inclinations, the time lag is rather small. The continuum is directly seen by the observer (zero time-lag) and polarized radiation mainly scatters on the inner disk funnel before reaching the observer, lagging the continuum by about 10 months. In the infrared band, the uniformly filled model shows the longest times lags but the increase with respect to the other models between 0° and 45° orientations is merely detectable. It is only at inclinations larger than 45° that the five models become truly unique in terms of temporal signatures. When the dust density increases with radius, the time-lag abruptly increases when the inclination becomes slightly larger than 45° and then becomes stable. Since there is a very small number of photons that can escape from the densest outer layers of the disk (see the flux plot), most of the radiation detected at those angles is due to the backscattering of photons onto the opposite disk edge. The photon travel length being almost similar at all edge-on inclinations, the time-lag stabilizes at 400 – 600 months. A model with a constant-density dust prescription has a similar behavior but the time-lags are less important since

radiation faces a constant, high optical depth and thus scatters many times before escaping but is not trapped in the outer regions, in contrast with the previous cases. The time-lag slightly drops at perfect equatorial inclinations since photons that have backscattered on the opposite disk funnel are not longer able to reach the observer and thus do not delay the averaged time response. Finally, for models with decreasing radial dust densities, time-lags remain quite constant before and after the transition angle, solely showing a small increase at inclinations larger than 70° . This is also due to the amount of backscattered photons that outnumber those that have traveled through the equatorial plane (i. e. with a smaller time-lag).

We finally note that the time-lags differ in the near-infrared and the optical/ultraviolet bands, when energetic radiation can penetrate further in the dust material. For models with denser dust layers close to the source, IR photons mainly scatter onto the dust funnel while UV photons penetrate more easily in the material, increasing their time-lag. The change in waveband affects the three other models in the opposite way: their time-lag at polar views is lower. This is due to the combination of albedo and scattering/absorbing cross sections variations, as explained above.

Summarizing what we have found for the plain flared disks, we have shown that different dust prescriptions result in specific inclination-dependent attenuations of the flux. If the dust layers become thicker with increasing distances from the central source, less photons are detected towards the equatorial regions. It is not the case for the other configurations that allow more radiation to be detected at high inclinations. The variations of the polarization degrees and angles are also very characteristic; the polarization is maximum for models with radially-increasing dust densities. Those same models also provide the highest time-lags at equatorial views at all three wavebands. We note that the differences are less pronounced for type-1 (pole-on) inclinations, where the structure of the equatorial distribution of dust has a lesser impact on the averaged time lags. This prevents a very clear determination of the morphology of the disk from time reverberation studies that can be achieved only for low inclination objects, showing the importance of coupling timing and polarimetric studies to break degeneracies.

3.2. Fragmented disks with constant-radius clouds

Our second series of models focuses on fragmented disks with clumps of equal sizes. We examine in Fig. 7, Fig. 8 and Fig. 9 a model where the optical depth is the same for all clumps (fixed to 50 in the V-band, model 3) and a model where the dust opacity varies with radial distance from the central source (model 4). In the later case, we consider the same four dust prescriptions (a), (b), (c), and (d) as previously (see Fig. 2).

The normalized photon fluxes are maximum at polar inclinations as discussed in the previous section. However the flux attenuation due to obscuration is much less important at edge-on orientations. The clumpy structure of the disk is responsible for gaps between the cloudlets, allowing radiation to escape more easily thanks to multiple scattering. The interclump medium is pure vacuum here, but similar results are found for a clumpy two-phased medium with high-density clumps embedded in a low-density interclump dust (Stalevski et al. 2012). The flux attenuation is model-dependent. In the infrared, fluxes along the equator are smaller by about one order of magnitude than the polar value for models with exponential opacity distributions, and by almost two orders of magnitude in the linear case. The constant-density model (model 3) presents the lowest equatorial

flux. We therefore see that the dust distribution has a profound impact on the quantity of transmitted flux at edge-on views. The photon fluxes are almost inclination-independent once the observer's line-of-sight has crossed the disk horizon, with a smooth transition between $i = 35^\circ$ and $i = 50^\circ$. The geometry of the system drives the shape of the curves and all five models appear similar (albeit their flux levels). Moving towards shorter wavelengths has no impact on the shape of the curve but the derived photon flux at edge-on inclinations is slightly different due to the combined effect of albedo and cross-section. All models appear to give equivalent fluxes along the equatorial plane, between one and two orders of magnitude less than along the pole.

The polarimetric results (right panels of Figs. 7, 8 and 9) are very different from the plain flared disk models, and are also characteristic of the model used. Whereas the infrared polarization degree along polar directions for the plain disk cases can reach $\sim 0.25\%$, here it is at best 0.17% for the model with an exponentially-increasing dust opacity with radial distances from the source (model 4b). For this model, radiation mainly scatters in the equatorial plane until reaching the outer part of the disk. At this location, the dust density is maximum and the resulting polarization position angle is equal to 90° . A clumpy disk with a linear increase of dust opacity with distance (model 4a) also presents a 90° polarization angle when observed edge-on, but its polarization degree is smaller. The seemingly chaotic variations of the polarization angle are due to the clumpiness of the medium and not to insufficient statistics. For the other models (model 3 and models 4(c-d)), the level of linear polarization at polar inclinations is very low due to the inefficiency of the clumpy disk to scatter photons towards the observer. The resulting polarization angle is 0° . This efficiency increases with inclination as the observer's line-of-sight becomes obstructed by clumps. The infrared polarization degree sharply rises up to 18% in the case of constant-density clumps (model 3). For dust densities that decrease linearly (model 4c), the maximum polarization degree is 15% and for the last two models that are much less capable of absorbing/scattering radiation, the maximum polarization is about 10% . For all models, the polarization position angle is equal to 0° between $40^\circ - 60^\circ$ inclinations since polar scattering dominates. At larger inclinations, there is a rotation of the polarization angle for all models: the polarization angle becomes parallel while the polarization degree decreases. Scattering along the equatorial plane is now the easiest path to escape the clumpy dusty disk. This results in low infrared polarization degrees with 90° polarization position angles. This behavior was already revealed in Marin et al. (2015) and Marin & Schartmann (2017) for constant-density clumpy models but we now show that their results also apply to more complex dust distributions. As for the plain disk discussed in Sect. 3.1, we find a wavelength-dependent polarization variation, the maximum polarization degree of the models decreasing for shorter wavelength. This is due to smaller scattering cross section when the photon energy increases, which allows radiation to travel more easily through the dusty structure without interacting.

The time-lags results (bottom-left panel of Figs. 7, 8 and 9) are also very different from their plain disk counterparts. Even at polar inclinations the time needed to escape from the dusty structure is large for photons that have scattered only once or twice. Since the medium is clumpy, radiation has traveled far inside the disk before being scattered towards the observer. The time-lag is thus about 10 times larger than for a plain disk, where radiation mainly scatters inside the dust funnel. Note that this is not due to a higher albedo but rather to the existence of vacuum between the cloudlets that allows radiation to travel without being

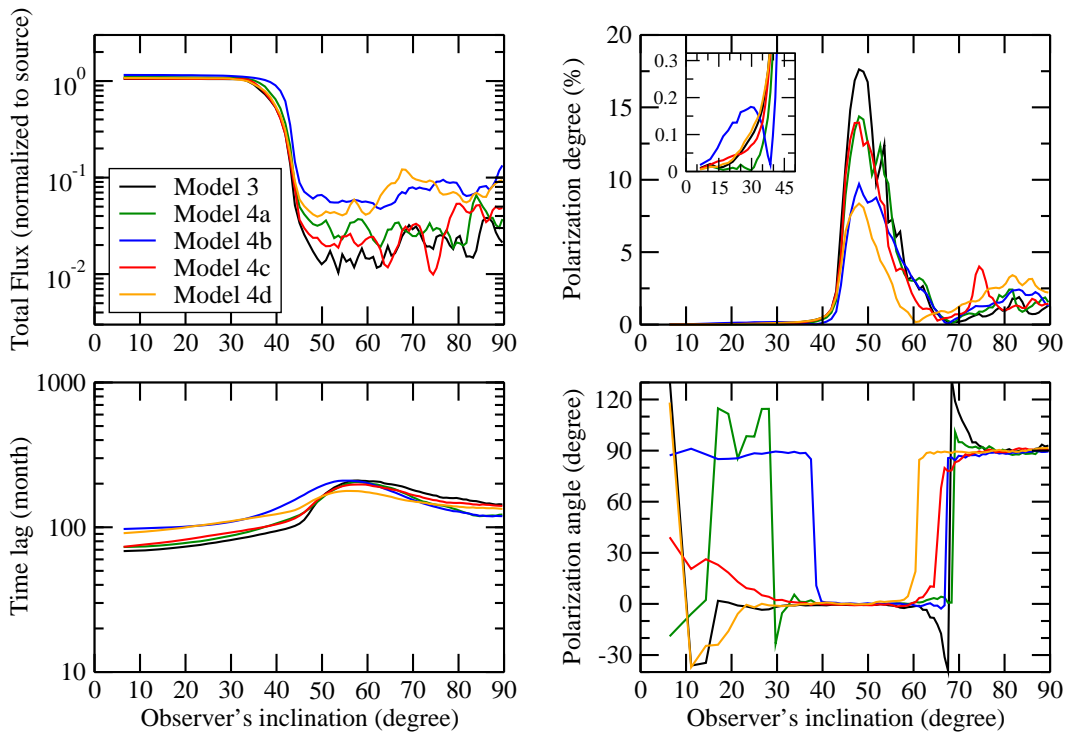


Fig. 7. Near-infrared ($10\,000\text{ \AA}$) total flux (normalized to the source emission), polarization degree, polarization angle and time-lag (normalized to the size of the disk) as a function of the observer's inclination. Five clumpy flared disk models with clumps of constant radius but different dust distributions are presented (see Sect. 2.1 for details).

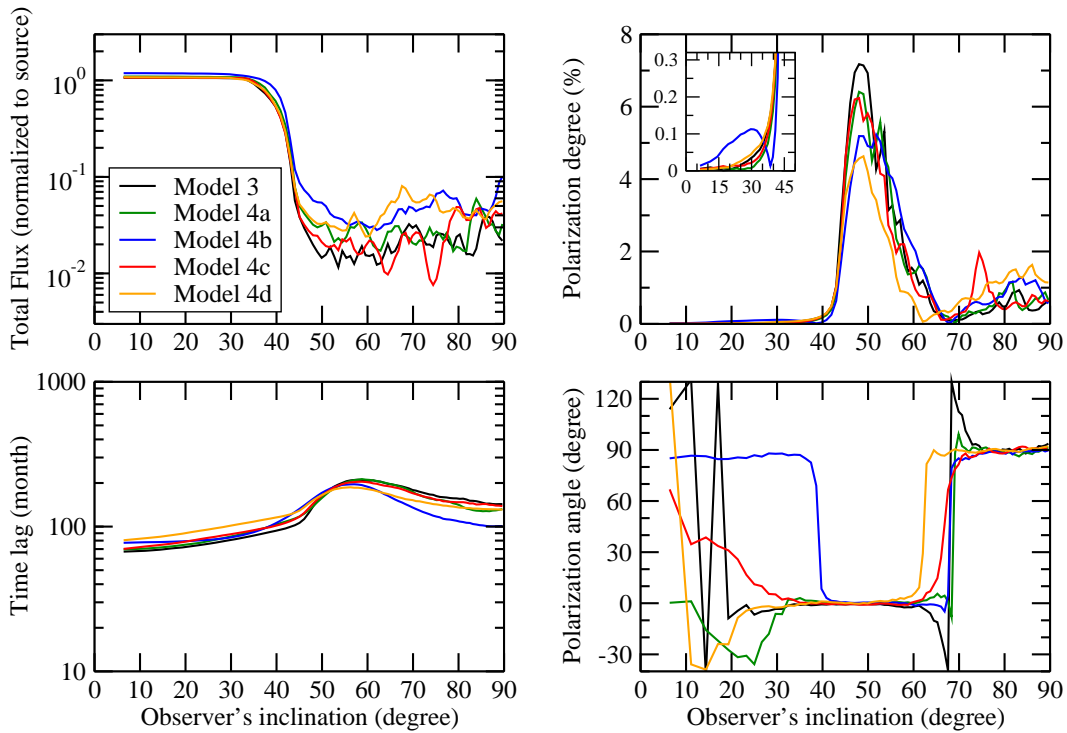


Fig. 8. Same as Fig. 7 but in the optical band (5500 \AA).

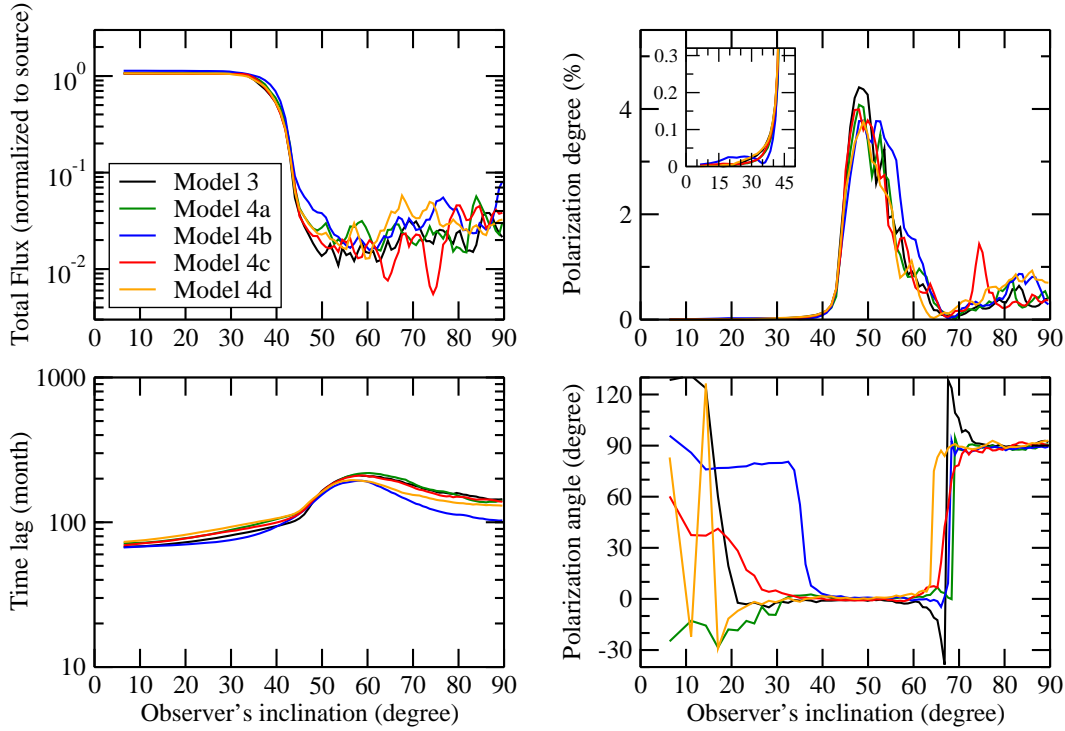


Fig. 9. Same as Fig. 7 but in the ultraviolet band (2000 \AA).

absorbed. Model 4(b) presents the highest time-lags due to the exponential increase of optical depth with distance to the source. Only the outer parts of the disk are filled with high density, high opacity clumps. Photons thus travel a large distance before being scattered towards the observer. All other models show approximately equal time-lags, the lowest values being obtained for the constant-density sphere model (model 3). When obscuration becomes efficient (at inclination larger than 45°), the time-lag values increase by a factor ~ 2 depending on the model. This increase correlates with the flux attenuation and the rise of polarization degree observed in other panels. This is a clear indication for a maximum efficiency of obscuration and a large number of scattering events. Finally, when equatorial scattering dominates at edge-on inclinations, the time-lags decrease but stay larger than at polar angles. The dependence of time-lags with inclination is very similar at shorter wavelengths, with only a marginal quantitative decrease.

We conclude that, for clumpy disks with constant radius spheres, the attenuation between a polar and an equatorial inclination is not very effective. The transition between the two extreme inclinations is smooth and operates around the half-opening angle of the dusty structure. If the half-opening angle is not the same for all observable sources, then it becomes impossible to distinguish between different dust stratifications. However polarimetry can reveal the distribution of dust with respect to the central source as the polarization degree reaches different maxima for different cases. The best waveband for observing the polarimetric signatures of clumpy tori is in the near-infrared where polarization levels larger than 10% are expected for a narrow range of inclinations. Different dust structuring also imprint the polarization position angle with specific values at polar orientations. Finally, reverberation measurements hardly differen-

tiate between the different models since they all give the same inclination-dependent curves. The time-lags they produce are too similar to be clearly distinguished.

3.3. Fragmented disks with variable clump sizes

Our last set of models is presented in Figs. 10, 11 and 12. In this case, the dusty disk is clumpy and the clump radii increase with distances from the central source. We arbitrarily set the radius of clumps situated at the outer part of the structure to be ten times larger than clumps located at the inner edge. Similarly to Sect. 3.1 and Sect. 3.2, we examine a model where the dust opacity is constant for each clump (model 5) and four models (6(a) – 6(d)) where the dust opacity varies with radial distance from the source (see Fig. 2).

The normalized total flux appears to be constant at polar viewing angles since, as previously, it is dominated by direct flux from the central source. At low angles, the fluxes are inclination- and model-independent. Differences only appear when the observer's line-of-sight crosses the dusty disk. In the case where the opacity exponentially decreases with distance, the disk does not efficiently block radiation at equatorial viewing angles. The flux has decreased by only one order of magnitude. The gaps between the clouds and the presence of low opacity, large dust cloudlets at the outer disk radius do not allow for a large obscuration. If the dust opacity decreases linearly, obscuration is slightly more efficient since the cloud opacity is still higher than 10 (V-band) at 8 pc from the source (while it is about 2 – 3 in model 6(d)). If the disk is composed of low opacity inner (small) clouds and high opacity outer (large) clouds, radiation is more heavily absorbed. Fluxes are about four orders of magnitude lower

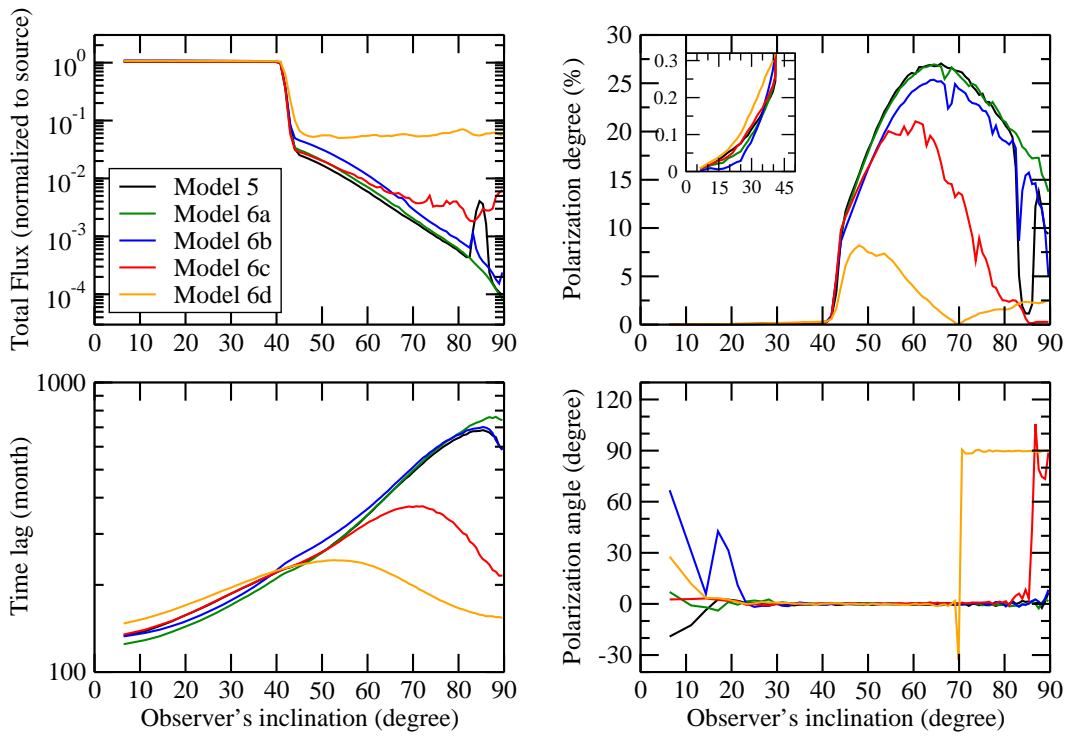


Fig. 10. Near-infrared ($10\,000\text{ \AA}$) total flux (normalized to the source emission), polarization degree, polarization angle and time-lag (normalized to the size of the disk) as a function of the observer's inclination. Five clumpy flared disk models with clumps of increasing radius and different dust distributions are presented (see Sect. 2.1 for details).

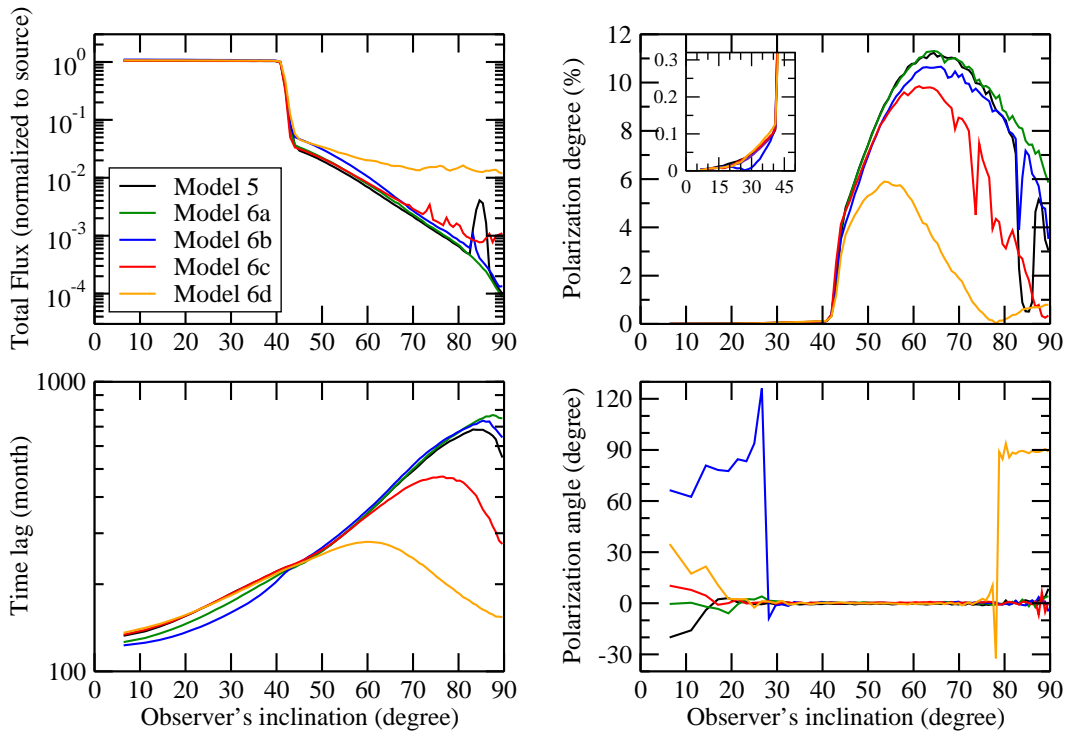


Fig. 11. Same as Fig. 10 but in the optical band (5500 \AA).

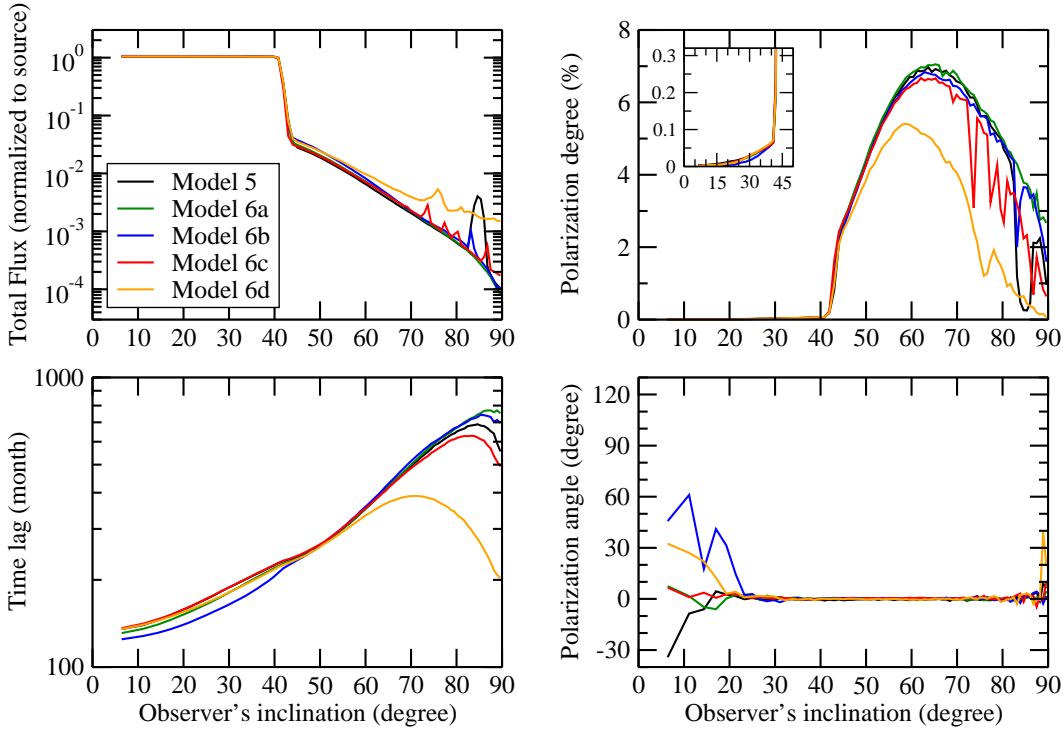


Fig. 12. Same as Fig. 10 but in the ultraviolet band (2000 Å).

at extreme equatorial inclinations for the three remaining models (models 5, 6a and 6b). The flux decrease with inclination is exponential for these three cases and the transition between unobscured and obscured sources is sharp at around the disk half-opening angle. The fluctuations we see in the flux curves are due to the distribution of clouds inside the model. For different realizations of clumpy disk models some features might appear if a given equatorial line-of-sight is not obscured by several optically thick clouds. This occurs, for example, in Fig. 10, models 5 and 6(c), at inclinations larger than 70° . The appearance of peaks and dips in the photometric curves are wavelength-dependent. As the photon energy decreases, radiation is less absorbed by dust grains and, if there is not enough dusty material to block radiation along a given direction, photon will escape more easily. This causes the low amplitude peaks of flux in the photometric curves observed in e.g. 6d which are visible in the ultraviolet but not in the infrared.

The polarimetric plots (right panels of Figs. 10, 11 and 12), show a sharp rise of polarization with increasing inclinations. At polar angles, the polarization degree exponentially rises up to 0.3%. The associated polarization position angle is 0° for all models in the near-infrared. This means that photons have not scattered much along the equatorial plane before escaping the system, but have instead mainly scattered on the large dust clumps located high above the equatorial plane, resulting in the characteristic perpendicular polarization angle. When the observer's line-of-sight becomes obstructed by dust, the polarization degree sharply rises since polar scattering clearly dominates over unpolarized emission from the (now) obscured source. Models with decreasing optical depth with radial distances from the center (6c,6d) have the lowest polarization degrees, since photons easily escape from the system, and therefore

do not carry large scattering-induced polarization. This effect is even more pronounced at equatorial inclinations when scattering along the equatorial plane dominates over polar scattering, resulting in a rotation of the polarization position angle for the two aforementioned models. The polarization degree thus shows dips, with minima associated to the rotation of the polarization angle. The case is slightly different for the other three models (5, 6a, 6b). Their polarization degree is as high as 25% and it is always associated with a perpendicular polarization position angle. For increasing inclinations the polarization degree regularly decreases for the same reason as above but since obscuration by large, optically thick, outer clumps is more efficient, equatorial scattering does not dominate and the polarization position angle remains equal to 0° . At shorter wavelengths, the results are similar but the polarization degrees are lower (down to 7% for the most polarized models in the ultraviolet band) as obscuration and depolarization through multiple scattering dominate over transmission.

The time-lags (bottom-left panel of Figs. 10, 11 and 12) are also quite different for different dust opacity prescriptions. The time-lags are similar for all models at polar inclinations, since they mainly result from scattering onto the large dust clouds at the outer radii of the fragmented disk. However, once the inclination is larger than 45° , the five models show different behaviors. Model 6(d) (density decreasing exponentially with distance) shows the lowest time-lags, with an infrared maximum around $i = 50^\circ$. The time-lag decreases at equatorial inclinations as photons preferentially escape by scattering close to the equatorial plane, carrying a smaller time delay than photons that have backscattered onto the disk funnel and then inside the cloud distribution. The same conclusions apply to a model with a linear decrease of density. It follows that a clumpy disk with increasing

cloud radii and decreasing optical depths would be, contrary to naive expectations, poor target for reverberation measurements. Better targets are models 5, 6(a) and 6(b). The time-lags increase with inclination, by factors up to up to 5. The presence of optically thick, large dust clouds in the outer borders of the system greatly facilitate time-lag observations since photons have to travel through the whole disk before being efficiently blocked and/or scattered by dust. This statement is even strengthened at shorter wavelengths where the time-lags are larger due to the ability of optical and ultraviolet photons to penetrate deeper in the dusty medium.

In summary, our last set of models has shown that clumpy disks with clumps of variable sizes and optical thickness have very distinctive features that are quite different for a variety of dust prescriptions. The importance of large and dense clumps at the outer edges of the disk is crucial for obtaining an efficient obscuration. They also enable large polarization degrees and time-lags. If the disk becomes more transparent with radial distances from the source, obscuration is less efficient and we observe a rotation of the polarization angle with increasing inclinations.

4. Discussion and observational prospects

We have shown that varying the morphology and/or the distribution of dust density in equatorial dusty structures has a profound impact on the observational properties (total flux, polarization degree and angles, time-lags) we have considered. The flux detected at equatorial inclinations is very sensitive to the structure of the disk: uniform or fragmented media result in flux levels that can be orders of magnitude different from those observed at polar viewing angles. Clumpy structures (either with constant or variable cloudlet radii) tend to be less efficient in blocking radiation along the equatorial plane unless the outer clouds are substantially bigger than the inner clouds. The resulting polarization is also distinctively different between the three morphologies and we found it to be much more sensitive to the radial distribution of dust than the photometric marker. The polarization degree is inclination-dependent and varies together with rotations of the polarization position angle that can trace the dust stratification. Finally, the averaged time-lags resulting from multiple scattering in different models is also a very distinctive signature that can probe the morphology of the scattering medium. Those two observational properties, polarization and time-lags, are the bases of the polarized reverberation mapping technique introduced by Gaskell et al. (2012).

4.1. Polarized reverberation mapping

By comparing the amplitude of variability of the polarized flux to the amplitude of variability of the total flux in a blue passband with effective wavelength of 3600 Å, Gaskell et al. (2012) found that the polarized flux of the Seyfert-1 NGC 4151 follows the total flux with a lag of 8 ± 3 days. This, together with the orientation of the position angle of the polarized flux, enabled to constrain the effective size of the unresolved equatorial scattering region of the AGN, most probably composed of electrons. This is the first and unique example so far illustrating the importance of polarized reverberation mapping in resolving the innermost structure of AGN. Achieving those observations is time consuming and required about seven years of monitoring the total and polarized fluxes of NGC 4151. In contrast with the work of Gaskell et al. (2012), who probed the inner broad line region, we have shown here that dust scattering results in longer timescales,

of the order of several months for type-1 (polar) inclinations. It is therefore very important to select the optimal wavebands before starting such long observational campaigns.

Our results indicate that the near-infrared band seems to be the best to search for high degrees of polarization, since photons are not energetic enough to travel far into the dusty medium; instead, they are reflected (the albedo is large) and do not penetrate much the disk, leading to high polarization degrees. This applies to either polar, intermediate or equatorial inclinations. However, the reader must bear in mind that thermal re-emission from dust and starlight dilution (from the host galaxy in the case of AGN) may also be strong enough to wipe out the polarization signature (Miller & Antonucci 1983). Hence, a more secure waveband to search for the polarization signal from dusty equatorial structures is ultraviolet, where starlight emission decreases in spiral and elliptical galaxies (Bolzonella et al. 2000).

The reverberation mapping technique requires to observe both the continuum and the reprocessed spectra; the central source must be directly visible and the line of sight must not cross the obscuring dusty torus. This limits us to polar viewing angles, for which the time-lags are the shortest. In the AGN context, this is beneficial since the averaged time delays between variations of the polarized flux and of the total flux can be of the order of months (see Fig. 3 for example). We compared our results to the ones obtained by Almeyda et al. (2017), who investigated the mid-infrared reverberation response of a clumpy torus, and found them to be in agreement with ours, even if the authors considered lower energies. Depending on the isotropic or anisotropic distribution of clumps in their torus models, Almeyda et al. (2017) found an averaged optical-to-infrared time-lag of 80 – 150 days (i.e. 2.6 – 4.9 months) at 3.6 μm . In comparison, our clumpy model with constant cloudlet radius and optical depth gives a time-lag of 3.9 months (cross-correlated between the total and polarized fluxes at 1 μm). Shorter delays, can be obtained in the ultraviolet band (a conclusion also shared by Almeyda et al. 2017).

We therefore conclude that polarized reverberation mapping is quite possibly better suited for ultraviolet/blue observations. The time-lags between the unpolarized continuum and the polarized reprocessed spectrum will be shortened, while the observed polarization degree will be less diluted by starlight contribution. The combination of the two techniques, leading to *polarized* time reverberation studies, will strongly help to break degeneracies. Our simulations suggest that much more sophisticated models are less easy to distinguish/constrain, but the combination of observables can still serve to rule out certain scenarios. The main difficulty here is that for low inclinations, the polarized fraction is small whereas for large inclinations, the unabsorbed, direct flux is severely reduced. Gaskell et al. (2012) have nevertheless clearly established the feasibility of such an observational study for the case of NGC 4151, but one has to remember that it took them about seven years to complete the observations. Multi-wavelength analysis such as radio observations to probe the kinematics and composition of the circumstellar/circumnuclear region or hard X-rays, which are much less absorbed/scattered than the optical, might be useful to narrow down the uncertainties. A detailed treatment of the problem is deferred to a forthcoming paper where we intend to construct artificial light curves in both total and polarized light to measure realistic time lags, including both dilution by the host, interstellar polarization and sophisticated transfer functions.

4.2. Towards more sophisticated models

We have shown that two dusty structures with the same geometry but different dust grain distributions (e.g. a linear increase and an exponential increase of opacity with radial distance from the central source) are distinctively different in terms of polarization and timing properties, see Fig. 12 for example. However, those differences are less likely to be detectable in terms of photometry, since almost all models give the same inclination-dependent trend in flux attenuation. To detect a radial stratification of dust, time-resolved polarimetry appears to be the solution but it is unclear that this conclusion would also applies for vertical stratifications and for chemical variations of the dust grains with distance from the source. It has been known for long that the dust composition and temperature of stellar nebulae varies with distance from its young star (Bally & Reipurth 2006); the same applies to galaxies, since the galactocentric dust mineralogy varies with distance and metallicity (Giannetti et al. 2017). We thus naturally expect circumstellar and circumnuclear dusty disks to be also more complex than considered here.

It is beyond the scope of this paper to consider all possible dust distributions with distance, altitude, temperature or metallicity. We have already proven that uniformly filled equatorial dusty structures give different polarimetric and timing outputs than structures with radial dust opacity gradients. However, in order to illustrate the complexity of the parameter space for filling the disk with dust, we show in Fig. 13 one realization of our numerical code for a clumpy disk with constant cloud radii in the case of a linear decrease of dust density with vertical distance from the equatorial plane. The simulation was achieved at $1 \mu\text{m}$ and results are shown in Fig. 13 using a plain solid black line. For comparison, we also show a model with the same parameters, excepts that the gradient is now radial instead of being vertical; the dust opacity linearly decreases with radial distance from the central source (black dashed line). As can be seen, the two configurations (vertical and radial variations of opacity) are almost indistinguishable in terms of photometry. The signal is the same at polar viewing angles and the obscured flux at equatorial orientations is equivalent. Differences can only be attributed to the random positions of the clouds. The unique true difference between the two models is the inclination angle at which the transition between the “unobscured” and “obscured” state occurs. The vertical opacity stratification configuration is similar to a configuration where an optically thin atmosphere lays on top of denser equatorial layers. Photons grazing the disk surface are less likely to be absorbed. It is only at a larger inclination, where the medium finally becomes optically thick, that the disk can efficiently block radiation. In terms of polarization we see that the inclination-dependent degree of polarization follows the same trend, but the maximum amount of polarization is only 11% instead of 14% at intermediate inclinations. The small bump of polarization observed at an inclination of $\sim 75^\circ$ is due to the random distribution of the clumps position in the disk. The polarization position angle is the only marker showing a distinctive difference between the two configurations. The polarization angle is 90° for $i = 0^\circ$, indicating that scattering mainly happens along the equatorial plane. In comparison, for a radial opacity stratification, the polarization angle is close to 45° since both equatorial and polar scattering are contributing. Here, the vertical stratification of dust density favors scattering along the equatorial plane where the disk is denser. For larger inclinations, the polarization angle rotates to 0° , as in the radial case, since backscattering on the disk funnel becomes important at those intermediate inclinations. It is only at large inclinations, when

the continuum is obscured and when backscattering is no longer dominant with respect to equatorial scattering, that the polarization angle switches to 90° . Similarly to the photometric results, the angle at which this transition happens is different from the radial stratification scenario. Finally, the inclination-dependent averaged time-lag is almost indistinguishable between the two cases since the geometry of the medium plays a more important role than its composition in time domain studies.

5. Conclusions

In this paper, we have shown that the morphology or the distribution of dust density of an equatorial dusty structure has a profound impact on the polarized signal and on the expected (averaged) time-lags. A plain uniform structure may have a similar behavior to that of a complex clumpy one in terms of flux attenuation but the polarization degree and angle would be significantly different. If the polarization signal from the equatorial dusty disk can be isolated from the central source or from additional components (which is more problematic in the case of AGN), it is possible, in principle, to distinguish between different models. In particular, the dust distribution inside a disk has a very clear inclination-dependent polarization signature. Since the inclination is not easy to determine from observations, coupling timing and polarimetric informations is crucial for determining the physical size of the unresolved region, together with its composition.

We also found that the ultraviolet/blue band is quite probably better suited for polarized time-reverberation studies. The polarization level due to dust scattering is not expected to be as high as in the near-infrared but the ultraviolet waveband should be less contaminated by external starlight and thermal re-emission. In addition, the time delays are expected to be slightly shorter in this waveband, allowing for less time-consuming observational campaigns. We intend to continue this study by applying cross-correlation methods to light curves obtained by our Monte Carlo method. We aim at reproducing the observed time-delays of NGC 4151 first, estimate the inclination of the AGN by testing all the possible orientations thanks to our numerical code, and then try to evaluate the existence of additional structures in the AGN by checking their influence onto the resulting polarization signal and time-delays.

Acknowledgements. The authors would like to thank the anonymous referee for useful suggestions that helped to improve this paper. This research has been supported by the French Programme National des Hautes Energies (PNHE). FM is grateful for CNES funding under the post-doctoral grant “Probing the geometry and physics of active galactic nuclei with ultraviolet and X-ray polarized radiative transfer”. APRL acknowledge support from the CONICYT BECAS Chile grant no. 72150573.

References

- Almeyda, T., Robinson, A., Richmond, M., Vazquez, B., & Nikutta, R. 2017, *ApJ*, 843, 3
- Andrews, S. M., Wilner, D. J., Zhu, Z., et al. 2016, *ApJ*, 820, L40
- Antonucci, R. 1993, *ARA&A*, 31, 473
- Antonucci, R. R. J. & Miller, J. S. 1985, *ApJ*, 297, 621
- Apai, D., Pascucci, I., Brandner, W., et al. 2004, *A&A*, 415, 671
- Bally, J. & Reipurth, B. 2006, *The Birth of Stars and Planets*
- Beckert, T., Driebe, T., Hönig, S. F., & Weigelt, G. 2008, *A&A*, 486, L17
- Beckwith, S. V. W. & Sargent, A. I. 1996, *Nature*, 383, 139
- Beckwith, S. V. W., Sargent, A. I., Chini, R. S., & Guesten, R. 1990, *AJ*, 99, 924
- Bilíková, J., Chu, Y.-H., Gruendl, R. A., Su, K. Y. L., & De Marco, O. 2012, *ApJS*, 200, 3
- Bolzonella, M., Miralles, J.-M., & Pelló, R. 2000, *A&A*, 363, 476
- Burtscher, L. & Tristram, K. R. W. 2013, *The Messenger*, 154, 62

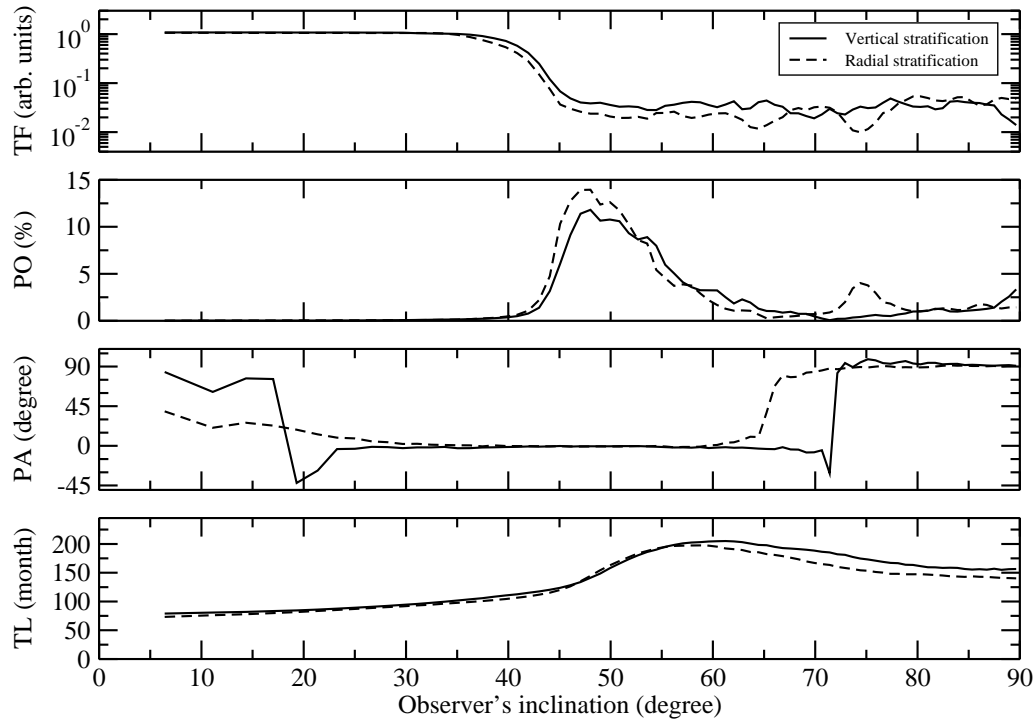


Fig. 13. Comparison between a radial (solid dashed line) and a vertical (solid plain line) dust stratification in a clumpy equatorial flared disk with spheres of constant radius. The variation of the dust density is linear and decreases from the center of the model (first case) and from the equatorial plane (second case). The top panel shows the normalized photon flux at $1 \mu\text{m}$, the second panel is the polarization degree, the third panel is the polarization position angle, and the last panel is the time-lag as a function of the system inclination.

- Chu, Y.-H., Su, K. Y. L., Bilikova, J., et al. 2011, *AJ*, 142, 75
 Clayton, G. C., De Marco, O., Nordhaus, J., et al. 2014, *AJ*, 147, 142
 Czerny, B. & Hryniewicz, K. 2012, in *Journal of Physics Conference Series*, Vol. 372, *Journal of Physics Conference Series*, 012013
 D'Alessio, P., Calvet, N., Hartmann, L., Lizano, S., & Cantó, J. 1999, *ApJ*, 527, 893
 D'Alessio, P., Cantó, J., Calvet, N., & Lizano, S. 1998, *ApJ*, 500, 411
 Dubrulle, B., Morfill, G., & Sterzik, M. 1995, *Icarus*, 114, 237
 Dullemond, C. P., Henning, T., Visser, R., et al. 2007, *A&A*, 473, 457
 Eisner, J. A., Hillenbrand, L. A., White, R. J., et al. 2007, *ApJ*, 669, 1072
 Farihi, J., Jura, M., & Zuckerman, B. 2009, *ApJ*, 694, 805
 Gaskell, C., Goosmann, R., Antonucci, R., & Whyson, D. 2004, in *Astronomical Society of the Pacific Conference Series*, Vol. 311, *AGN Physics with the Sloan Digital Sky Survey*, ed. G. T. Richards & P. B. Hall, 61
 Gaskell, C. M., Goosmann, R. W., Merkulova, N. I., Shakhovskoy, N. M., & Shoji, M. 2012, *ApJ*, 749, 148
 Giannetti, A., Leurini, S., König, C., et al. 2017, *A&A*, 606, L12
 Gledhill, T. M., Scarrott, S. M., & Wolstencroft, R. D. 1991, *MNRAS*, 252, 50P
 Gnedin, Y. N., Piotrovich, M. Y., Silant'ev, N. A., Natsvlshvili, T. M., & Buliga, S. D. 2015, *Astrophysics*, 58, 443
 Goosmann, R. W. & Gaskell, C. M. 2007, *A&A*, 465, 129
 Hillenbrand, L. A., Strom, S. E., Calvet, N., et al. 1998, *AJ*, 116, 1816
 Holwerda, B. W., Bianchi, S., Böker, T., et al. 2012, *A&A*, 541, L5
 Horne, K. 1985, *MNRAS*, 213, 129
 Jaffe, W., Meisenheimer, K., Röttgering, H. J. A., et al. 2004, *Nature*, 429, 47
 Jones, A. P. 2016, *Royal Society Open Science*, 3, 160224
 Kishimoto, M., Hönig, S. F., Beckert, T., & Weigelt, G. 2007, *A&A*, 476, 713
 Krolik, J. H. & Begelman, M. C. 1988, *ApJ*, 329, 702
 Li, A. 2007, in *Astronomical Society of the Pacific Conference Series*, Vol. 373, *The Central Engine of Active Galactic Nuclei*, ed. L. C. Ho & J.-W. Wang, 561
 Liu, J., Liu, Y., Li, X., et al. 2016, *MNRAS*, 459, L100
 López-Gonzaga, N. & Jaffe, W. 2016, *A&A*, 591, A128
 Marin, F. 2014, *MNRAS*, 441, 551
 Marin, F. 2016, *MNRAS*, 460, 3679
 Marin, F. & Goosmann, R. W. 2014, in *SF2A-2014: Proceedings of the Annual meeting of the French Society of Astronomy and Astrophysics*, ed. J. Ballet, F. Martins, F. Bournaud, R. Monier, & C. Reylé, 103–108
 Marin, F., Goosmann, R. W., & Gaskell, C. M. 2015, *A&A*, 577, A66
 Marin, F., Goosmann, R. W., Gaskell, C. M., Porquet, D., & Dovčiak, M. 2012, *A&A*, 548, A121
 Marin, F. & Schartmann, M. 2017, *A&A*, 607, A37
 Marinucci, A., Bianchi, S., Matt, G., et al. 2016, *MNRAS*, 456, L94
 Marsh, T. R. & Horne, K. 1988, *MNRAS*, 235, 269
 Meisenheimer, K., Raban, D., Tristram, K., et al. 2008, *The Messenger*, 133, 36
 Miller, J. S. & Antonucci, R. R. J. 1983, *ApJ*, 271, L7
 Mundy, L. G., McMullin, J. P., Grossman, A. W., & Sandell, G. 1993, *Icarus*, 106, 11
 Nenkova, M., Ivezić, Ž., & Elitzur, M. 2002, *ApJ*, 570, L9
 Netzer, H. 2015, *ARA&A*, 53, 365
 Pinte, C., Harries, T. J., Min, M., et al. 2009, *A&A*, 498, 967
 Pollack, J. B., Hollenbach, D., Beckwith, S., et al. 1994, *ApJ*, 421, 615
 Sazonov, S., Churazov, E., & Krivonos, R. 2015, *MNRAS*, 454, 1202
 Scholz, A., Xu, X., Jayawardhana, R., et al. 2009, *MNRAS*, 398, 873
 Schräpler, R. & Henning, T. 2004, *ApJ*, 614, 960
 Siebenmorgen, R., Heymann, F., & Efstathiou, A. 2015, *A&A*, 583, A120
 Stalevski, M., Fritz, J., Baes, M., Nakos, T., & Popović, L. Č. 2012, *MNRAS*, 420, 2756
 Su, K. Y. L., Chu, Y.-H., Rieke, G. H., et al. 2007, *ApJ*, 657, L41
 Vicente, S. M. & Alves, J. 2005, *A&A*, 441, 195
 Walker, C., Wood, K., Lada, C. J., et al. 2004, *MNRAS*, 351, 607
 Wolf, S. & Henning, T. 1999, *A&A*, 341, 675